Metals and Materials International
https://doi.org/10.1007/s12540-021-01164-7

Role of Alloying Composition on Mechanical Properties of CuZr Metallic Glasses During the Nanoindentation Process

Saade Abdalkareem Jasim[1] · Muneam Hussein Ali[2] · Zaid Hameed Mahmood[3] · Mohammad Rudiansyah[4] · Forat H. Alsultany[5] · Yasser Fakri Mustafa[6] · Montather F. Ramadan[7] · Aravindhan Surendar[8]

Received: 28 October 2021 / Accepted: 26 December 2021

Abstract
This paper aims to indicate the role of alloying composition on the nanomechanical properties of metallic glasses (MGs). For this purpose, the molecular dynamics simulation of nanoindentation process was performed for a wide range of Cu–Zr glassy compositions. The results indicated that the yielding event enhanced with the rise of Cu content; however, there existed an optimized composition for the maximum hardening effect in the system. The investigation on the evolution of shear bands also showed that the formation of pile-ups around the indentation site and the propagation of dominant shear bands into the glassy structure occurred in the Cu-rich MGs. On the other side, the increase in Zr content led to the creation of a net-like shear arrangement under the indented site. Moreover, the Voronoi tessellation analysis indicated that the decreasing/increasing rate of polyhedron types during the indenting process strongly relied on the alloying compositions.

Keywords Metallic glass · Molecular dynamic simulation · Nanoindentation · Plasticity

1 Introduction

Owing to their long-range random atomic arrangements, metallic glasses (MGs) represent superior physical and mechanical properties [1–3]. However, their unique deformation mechanism impedes the evaluation of plastic behavior and mechanical properties under an external loading [4, 5]. In general, the creation of shear bands along the shear planes leads to the localized deformation and subsequent catastrophic failure of glassy alloys [6–8]. The formation of shear bands within the glassy matrix is correlated to the activation and percolation of nanoscale shear transformation zones (STZs) [9–12]. Many other aspects of shear events such as interaction of STZs, nucleation and propagation of shear bands are also main items affecting the ductility and failure mechanism of MG alloys [13, 14].

The nanoindentation study, including the experimentations and simulations, has been one of the most efficient methods for characterizing the mechanical properties and shear-banding events in the glassy alloys [15–18]. Multiple investigations have been conducted by the nanoindentation technique to indicate the effects of loading parameters and materials properties on the deformation behavior of MGs. For example, Huang and Yan [19] performed the nanoindentation test under different spatial intervals and found that the alteration of interval led to a wide range of shear band propagations such as intersections, suppression and narrowing modes. They also reported that the increase in the loading rate of indenting test led to the attenuation of serrated flow sizes [20]. Li et al. [21] demonstrated that the hydrogen

✉ Aravindhan Surendar
Surendararavindhan@ieee.org

1 Medical Laboratory Techniques Department, Al-Maarif University College, Ramadi 31001, Iraq

2 Al-Nisour University College, Baghdad, Iraq

3 Department of Chemistry Sciences, College of Science, Diyala University, Baqubah, Iraq

4 Division of Nephrology & Hypertension, Department of Internal Medicine, Faculty of Medicine, Universitas Lambung Mangkurat, Ulin Hospital, Banjarmasin 70123, Indonesia

5 Medical Physics Department, Al-Mustaqbal University College, Hillah 51001, Iraq

6 Department of Pharmaceutical Chemistry, College of Pharmacy, University of Mosul, Mosul 41002, Iraq

7 Scientific Research Center, Al-Ayen University, Thi-Qar, Iraq

8 Department of Pharmacology, Saveetha Dental College and Hospital, Saveetha Institute of Medical and Technical Sciences, Chennai, India

Published online: 08 February 2022

addition into the Zr-based MG altered the mechanism of plasticity, so that the flow serrations became smooth with the increase of hydrogen content. In another work, it was unveiled that the Sn minor addition into the TiZrHfCuBe MG increased the number of shear events and declined the size of STZ regions, which could be attributed to the positive mixing enthalpy between the Cu/Be and Sn elements [22]. Considering the Berkovich nanoindentation method, it was also found that there was a close relation between the residual projected region and the shear band circles in the MG samples [23]. Under the nanoindentation test, Gao et al. [24] detected a distribution of trimodal shear band nucleation, which was associated with the types of characteristic relaxation behavior. Molecular dynamics (MD) simulation of nanoindentation test also elaborated the features of atomic rearrangement and nanoscale plasticity in the MGs. Wu et al. [25] demonstrated that the stress fluctuation occurred in the small aspect ratio of MG pillars; while, the large aspect-ratio pillars exhibited a buckling deformation mode with sudden stress drop during the nanoindentation test. In another work, it was found that the rise in the temperature of indenting process led to the increment of elastic modulus; whereas, the hardness tended to show a decreasing trend [26]. Zhao et al. [27] detected a hardening effect in the indented samples, which were treated by a pre-strain compressive force.

Although several works have studied the mechanical response of MGs under the external loadings, there is no comprehensive MD investigation regarding the identification of glass composition effects on the mechanical properties and plastic deformation mechanism of MGs during the indenting process. Hence, this work aimed to implement the MD simulation of nanoindentation in a wide range of CuZr compositions to find that how the initial structure determines the eventual properties of glassy material.

2 Computational Method

The MD simulation was performed by the large-scale atomic massively parallel simulator (LAMMPS) and embedded atom method (EAM) potential was applied to define the interplays between Zr and Cu atoms in the system [28]. The MG cells with size of $15 \times 15 \times 5$ nm^3 and chemical compositions of $Cu_{50}Zr_{50}$, $Cu_{54}Zr_{46}$, $Cu_{60}Zr_{40}$ and $Cu_{64}Zr_{36}$ were constructed through a melt-quenching technique under the cooling rate of 1×10^{10} K/s. It is worth-mentioning that the atomic systems, containing Zr and Cu atoms, were randomly configured at 300 K and then heated up to 2000 K following a 1-ns relaxation stage and a quenching event to obtain a glassy system at 300 K. The prepared cells were then replicated to produce larger cells with dimensions of $60 \times 45 \times 30$ nm^3. To remove the interface effects resulted from the replication process, a relaxation treatment was performed at 600 K for 2 ns and then the large cell was cooled to the room temperature (300 K) under the rate of 1×10^{10} K/s. It should be noted that the periodic boundary conditions (PBCs) in three directions were considered for the simulation. Moreover, the simulation time of 1 fs was set for an individual step and the control of temperature and pressure was carried out under the isothermal-isobaric NPT ensemble through Nose–Hoover thermostat and barostat, respectively [29].

The MD simulation model of nanoindentation is schematically presented in Fig. 1. As observed, a virtual spherical indenter with the radius of 10 nm was applied for the indenting process. In general, the MG substrate contains three types of atoms, namely Newtonian atoms, boundary atoms and the thermostat ones [26, 30]. At the bottom of the substrate, a 1-nm layer composed of boundary atoms is considered to avoid any movement during the indenting process. The 1.5-nm layer with the thermostat atoms is located at the top of the boundary atoms; while the upper side of substrate includes the atoms with the motion principle according to the classic Newton second law. The temperature of substrate is initially 300 K; however, the Langevin thermostat dissipates the exerted heat to ensure the temperature stability during the indenting process. The velocity-Verlet algorithm with a time step of 2 fs was used to integrate the Newton's equation of atomic movement in the system. The x and y directions were controlled by the periodic boundary conditions [27, 31]. It should be noted that the sample was firstly relaxed for 3 ps using canonical ensemble. At the beginning of indenting process, the indenter presses the surface

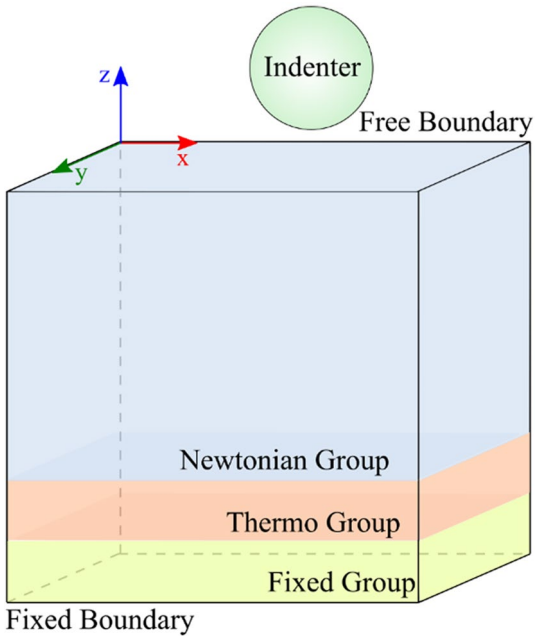

Fig. 1 Schematic of indentation loading on the MG surface

of substrate under the velocity of 80 m/s. The high velocity of indenting process is due to the computational limitations in the MD simulation, as also reported in other works [32, 33]. The embedded atom method potential with parameters extracted from ref. [28] was employed to model the atomic interactions. Each atom (i) contains a total energy based on the following equation [26]:

$$E_i = F_\alpha\left(\sum_{j\neq i}\rho_{\alpha\beta}(r_{ij})\right) = \frac{1}{2}\sum_{j\neq i}\varphi_{\alpha\beta}(r_{ij}) \quad (1)$$

F introduces the embedding energy and ρ defines the atoms' electron density. Pair potential interaction parameter is introduced by the φ symbol and the element type parameter of atoms i,j introduced by α and β. The repulsive force between the substrate and the indenter is calculated as follows [34]:

$$V(r) = A\theta(R-r)(R-r)^3 \quad (2)$$

In which r is the distance of atom to the center of indenting tool with R radius. θ(R − r) explains the standard step function and A defines the force constant. It is worthmentioning that the indenter is considered as a rigid solid (diamond) with no possible abrasion or deformation under the evolution of nanoindentation. Moreover, the substrate/indenter connection is defined by the Lennard–Jones (L–J) potential [35, 36]:

$$E = 4\varepsilon\left[\left(\frac{\sigma}{r}\right)^{12} - \left(\frac{\sigma}{r}\right)^{6}\right](r < r_c) \quad (3)$$

The interaction between substrate atoms and the indenter atoms is introduced by the energy parameter ε. Moreover, the distance between the indenter atoms and the substrate atoms is defined by parameter "r". Using the Lorentz–Berthelot mixing rules, the parameters of L–J equation were calculated and used in the MD model [26, 37].

3 Results and Discussion

The simulation of indentation process on the samples was performed and the attained force–displacement (P–h) curves are presented in Fig. 2a. One can see that the first pop-in sites, as the sign of yielding initiation, indicated a decreasing trend with the rise in the Zr content. However, it was detected that the whole position of P–h curves exhibited a different trend, so that an optimized Cu/Zr content is required for the maximum position (see Fig. 2b, c). It is believed that the higher position of curves is indicator of "hardening effect" in the MGs [27], while the first pop-in sites define the yielding initiation [8, 27, 38, 39]. Hence, one can conclude that there exists no proportional relation between the hardening and yielding phenomena in the CuZr MGs. With the increase in Cu concentration from 50 to 60 at.%, the indentation force becomes larger at the same indentation depth and afterwards, a slight decrement was detected in the $Cu_{64}Zr_{36}$ MG. It is also observed that the increase in the Cu/Zr ratio leads to the appearance of a plateau region in the curves at the deeper penetration of indenter, where the indenting force reaches the maximum value. On the other side, the low Cu/Zr ratio creates a continuously increasing curve without formation of any plateau region (See Fig. 2a). The creation of plateau region means that the force remains constant with the increase in the indenting depth, suggesting that the shear banding events are dominated during the indenting process. Several studies revealed that the domination of shear banding facilitates the pile-up phenomenon around the indentation region and releases the internal stresses in the structure, so that a decrement or constancy in the indenting force is observed [16, 40]. Hence, it is derived that the plateau regions in the P–h curves are mainly correlated to the pile-up formation under the indenting process.

Although the P–h curves provide significant information regarding the strength features of MGs, more detailed

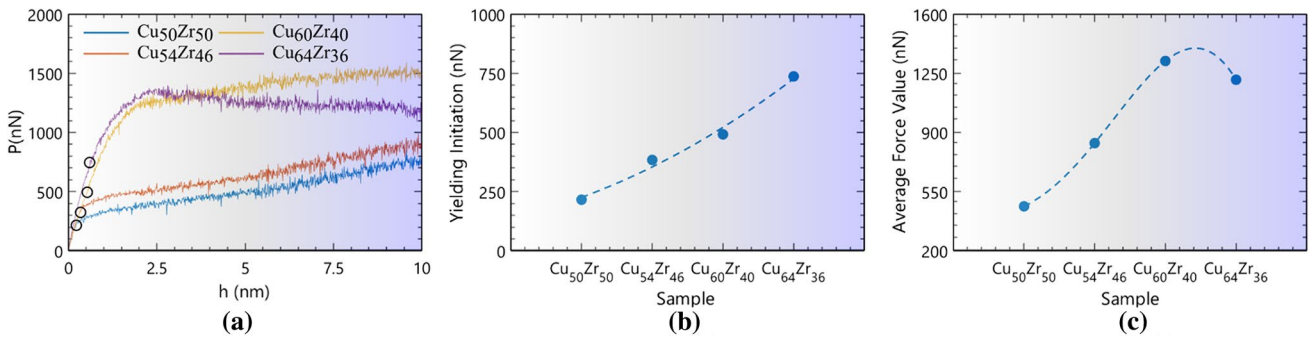

Fig. 2 **a** Load–displacement curves of samples, **b** yielding initiation, **c** average force (P) values as the function of alloying composition. The average force value is obtained from the indenting force of 4 to 10 nm displacement

investigation is necessary for characterizing the yielding behavior and plasticity evolution under the indenting process. To achieve this goal, a criterion should be considered for evaluating the atomic movement and the structural rearrangement in the glassy system. It was suggested that the atomic shear strain with the minimum value of 0.2 is responsible for the plastic deformation in the MGs [27, 41]. Consequently, the detection and assessment of these atoms, called large-strain (LS) atoms, reveal the nature of plasticity and yielding event under the nanoindentation test. Figure 3a illustrates the fraction of LS atoms during the indenting process for all the samples. The criterion for the plasticity initiation was the threshold fraction of 0.05% LS atoms in the glassy structure. The results indicated that the $Cu_{50}Zr_{50}$ MG shows a steady increment in the fraction of LS atoms. However, with the increase in the Cu content, the trend of SL evolution is divided into the two distinct parts. At the first part in the range of 0–5 nm depth of indentation, the SL fraction is gradually increased. Afterwards, a sharp increment is figured out at the high indenting depths (second part), which indicates that a sudden plastic deformation occurs in the glassy structure. Considering Figs. 2 and 3a, the abrupt rise of SL atoms in the Cu-rich MGs is related to the formation of dominant shear bands and localized pile-ups near the indentation region. Figure 3b demonstrates the engineering contact hardness of MGs, in which the hardness value was calculated through the equation H = P/2a, where the "P" is applied force and "a" defines the contact radius of indenter. As can be seen in the figure, the Cu-rich MGs, i.e. $Cu_{60}Zr_{40}$ and $Cu_{64}Zr_{36}$, exhibited a sharp increment of hardness at the beginning of indenting process; however, the further indentation was accompanied with a sudden drop in the curves. On the other side, the increase in Zr content leads to the gradual and stable enhancement of hardness under the evolution of indenting process. With the observation of hardness–depth (H–h) curve, one can also see that the rise of Cu content decreases the average hardness at the end of indenting process. This decrement is associated to the sudden softening of structure caused by the propagation of major shear bands [42, 43]. Similar to Fig. 2c, the average hardness value is obtained from the indenting force of 4 to 10 nm displacement and presented in Fig. 3c. The result demonstrated that the average hardness at the 4–10 nm depth exhibited a gradual increasing trend with the rise of Cu content (See Fig. 3c), while an optimized state was detected in Fig. 2c. This contradiction is owing to the fact that the hardness is evaluated based on the instantaneous radius of contact region, leading to a difference between the trends of average force and average hardness, especially for $Cu_{64}Zr_{36}$ and $Cu_{60}Zr_{40}$ MGs.

To better understand the mechanism of shear band formation under the nanoindentation process, the distributions of Von Mises shear strain should be evaluated. Figure 4 illustrates the maps of distributed Von Mises strain at the

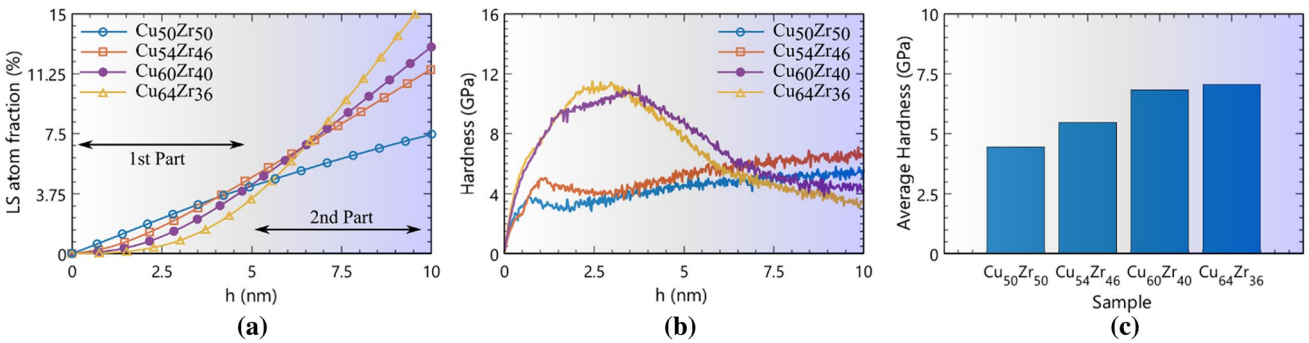

Fig. 3 **a** The variations of LS atoms in the indenting process, **b** the hardness value as a function of indenting depth, **c** average hardness values as the function of alloying composition. The average force value is obtained from the indenting force of 4 to 10 nm displacement

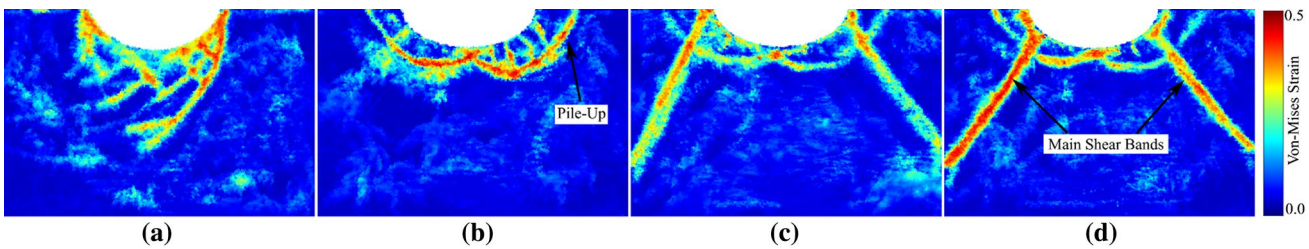

Fig. 4 The Von-Mises strain distribution in the indenting depth of 4 nm for **a** $Cu_{50}Zr_{50}$, **b** $Cu_{54}Zr_{46}$, **c** $Cu_{60}Zr_{40}$ and **d** $Cu_{64}Zr_{36}$

indenting depth of 4 nm for all the samples. At the first glance, one can see that the MD simulation reveals various shear banding morphologies in the glassy structure. In the $Cu_{50}Zr_{50}$, the shear bands exhibited a net-like configuration, in which the shear events are accumulatively propagated into the depth of glassy structure without any significant extension at the surface of sample. With the increase in the Cu content to 54 at. %, the extending degree of shear band generation is restricted to the vicinity of indented region, so that the shear bands are initiated from the indenter tip and then propagated to the surface from the both sides. This event shows the formation and evolution of pile-ups on the surface area, in which the indentation pit is surrounded by the visible deformation bands [44]. For the $Cu_{60}Zr_{40}$ and $Cu_{64}Zr_{36}$ MGs, the deformation is accompanied with the generation of pile-ups along with the dominant shear bands with a highly localized morphology deviated with the angle of 41°–47° into the samples. This result clearly indicated that the increase of Cu content leads to the localized shear events in the glassy structure, which is also confirmed by the appearance of plateau regions in the P–h curves (See Fig. 2).

To characterize the evolution of shear banding under the indenting process, the shear strain maps of $Cu_{50}Zr_{50}$ and $Cu_{60}Zr_{40}$ with different deformation modes are plotted and presented in Fig. 5. Considering the $Cu_{50}Zr_{50}$ MG, it was found that the shear bands are nucleated at the indentation depth of 0.5 nm below the indenter, meaning that the yielding event readily begins under the indenting process. This result is consistent with the P–h curves, in which the $Cu_{50}Zr_{50}$ MG exhibited the first pop-ins in the low forces. With the increase in the applied force, several shear events are distributed at the end of indenting region, so that a netlike shear banding phenomenon appears in the glassy structure. Finally, the increase of indenting depth leads to the prevailing of a shear band, which is responsible for further deformation in the sample. On the other side, the shear band evolution for the $Cu_{60}Zr_{40}$ MG is almost different. As observed, the nucleation of shear bands occurs in the indenting depth of 1.8 nm, showing the higher resistance of Cu-rich MG to the yielding event. It is also observed that the increment of applied load intensifies the shear banding and propagates it toward the edges of indenting region at the surface. Finally, the nucleated sites at the edges provide conditions for propagating of mature shear bands into the bulk of sample to create the localized deformation zones in the glassy matrix. Furthermore, it should be noted that the balance of elastic energy below the indented region leads to the release of energy from the glassy matrix into the mature shear bands, facilitating the propagation in the structure [26]. The dynamics and speed of shear band propagation also give important information regarding the mechanism of plastic deformation in the MGs. As depicted in other works [45, 46], the shear band propagation occurs in the milliseconds, leading to the sudden plastic deformation in the structure. In the glassy structures with low deformation capability, the STZs are rapidly percolated in the shear plane and created the shear band [47]. On the other side, the glassy structures with higher deformation capability are comprised of more potential sites for the STZ nucleation, leading to a severe interaction of shear events in the system. Moreover, the more loosely packed regions in this type of system facilitate the energy dissipation and impede the catastrophic shear band formation. As a result, the speed of shear band propagation decreases in the system. As measured in our work, the propagation speed of shear band is more than 1230 m/s in $Cu_{64}Zr_{36}$ alloy, demonstrating that an elastic-brittle deformation occurs in the Cu-rich sample. On the other hand, the propagation of dominant shear band in the $Cu_{50}Zr_{50}$ MG is near 990 m/s, implying the combination

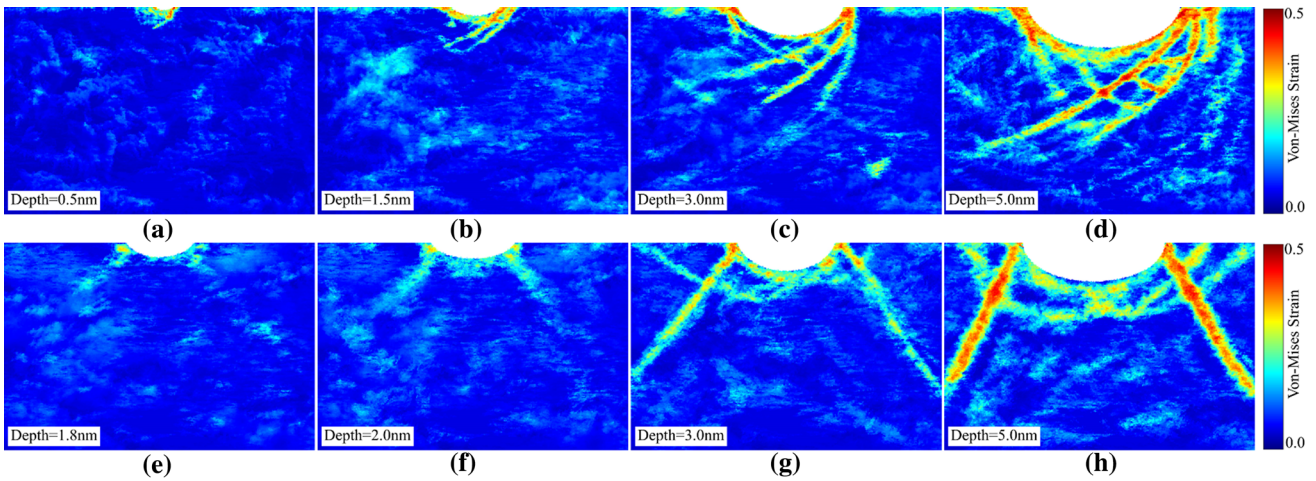

Fig. 5 The Von-Mises strain distribution under the evolution of indenting process for **a–d** $Cu_{50}Zr_{50}$, **e–h** $Cu_{60}Zr_{40}$

of elastic/plastic deformation under the indenting process, as also reported in other studies [27].

In general, there exists a wide range of deformation mechanism in the nanoindentation process from the elastic to the plastic transitions [48, 49]. When the deformation is in the elastic range, the induced energy is equally generated in the bulk of material. However, with the appearance of plastic deformation, the elastic energy of solid matrix is released through the plastic-strained regions in the form of thermal energy [50]. Under the evolution of indenting process, the ratio of elastic/plastic energies determines the deformation mode in the glassy alloy. In our study, the variations of total potential energy provide important information regarding the deformation mechanism. Considering this fact that the LS atoms are responsible for the irreversible deformation in the glassy structure, it is possible to evaluate the released energy from them to indicate the mechanism of shear banding in the glassy system. In an elastic regime, the induced energy gradually increases in the atomic configuration. However, the initiation of plastic deformation moderately enhances the released energy, which is due to the appearance of LS atoms. Moreover, the propagation of a sudden shear band with highly localized deformation under the indenting process leads to a sharp alteration in the potential energy, indicating the released energy level of the solid matrix in the vicinity of dominant shear band. As confirmed in other works [46, 51, 52], this event is the main reason for the extreme temperature rising in the shear band regions. In our study, we monitored the potential energy under the indenting test and plotted the energy alterations in the alloying systems (see Fig. 6). As observed, the $Cu_{50}Zr_{50}$ alloy shows a moderate energy increment, which is a sign of elastic–plastic deformation with fine shear banding events. However, a sharp increase was detected at the end of indenting test, implying the extension of shear bands in the structure. With the increase in the Cu content, the energy alteration exhibits a gradual increment, indicating that the deformation occurs in the elastic regime. Nevertheless, a sudden energy enhancement in the middle of indenting process reveals that the prevailing shear bands are created in the atomic configuration. Hence, from the energy point of view, it is concluded that the Cu-rich MGs exhibit a brittle mode with an initial elastic deformation and a subsequent localized plasticity. On the other side, the increase of Zr content in the MG alloy facilitates the creation of potential sites for the generation of more fine shear events, leading to a higher homogenous deformation.

The short range order (SRO) evaluation of structure determines the degree of atomic rearrangements and the response of glassy matrix to the creation of shear events under the indenting process. For this purpose, the Voronoi tessellation analysis was applied to identify the coordination polyhedrons in the system. Figure 7 indicates that the fraction of Cu-centered SROs decreases with the rise in the indentation depth, showing the creation of shear events and free volumes in the system [53, 54]. Nevertheless, one can notice that the decreasing trend relies on the chemical composition of glassy alloys. The detailed characterization of polyhedron fractions is given in Fig. 8. It was revealed that the trends of polyhedron evolution are altered under the rise of indenting depth. For the $Cu_{50}Zr_{50}$ MG, the polyhedrons ⟨0, 0, 12, 0⟩ and ⟨0, 2, 8, 1⟩ are the dominant SRO arrangements. During the indenting process, the fractions of these polyhedrons are moderately decreased, while there is a slight increment in the fraction of polyhedrons ⟨0, 3, 6, 3⟩ and ⟨0 1 10 2⟩ and ⟨0, 2, 8, 2⟩. On the other side, the increase in Cu content changes the initial fractions in the MG alloys. Nonetheless, the polyhedrons ⟨0, 0, 12, 0⟩ and ⟨0, 2, 8, 1⟩ are still the prevailing SROs in the material. It is also observed that the evolution of indenting process is accompanied with the intensification of decreasing trend in the polyhedron ⟨0, 0, 12, 0⟩ for the Cu-richer MGs. On the other side, the polyhedron ⟨0, 3, 6, 3⟩ remains stable and the polyhedral fractions of ⟨0 1 10 2⟩ and ⟨0, 2, 8, 2⟩ exhibited a sharper increment.

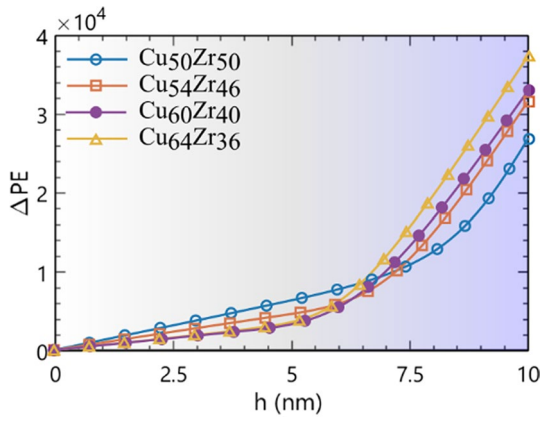

Fig. 6 Potential energy variations of all samples during indentation. The energy unit is eV

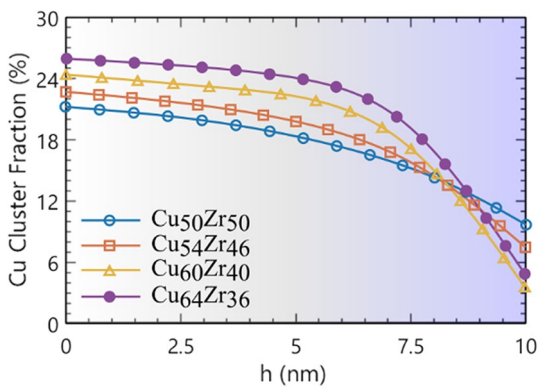

Fig. 7 The evolution Cu-centered SROs in the alloying systems

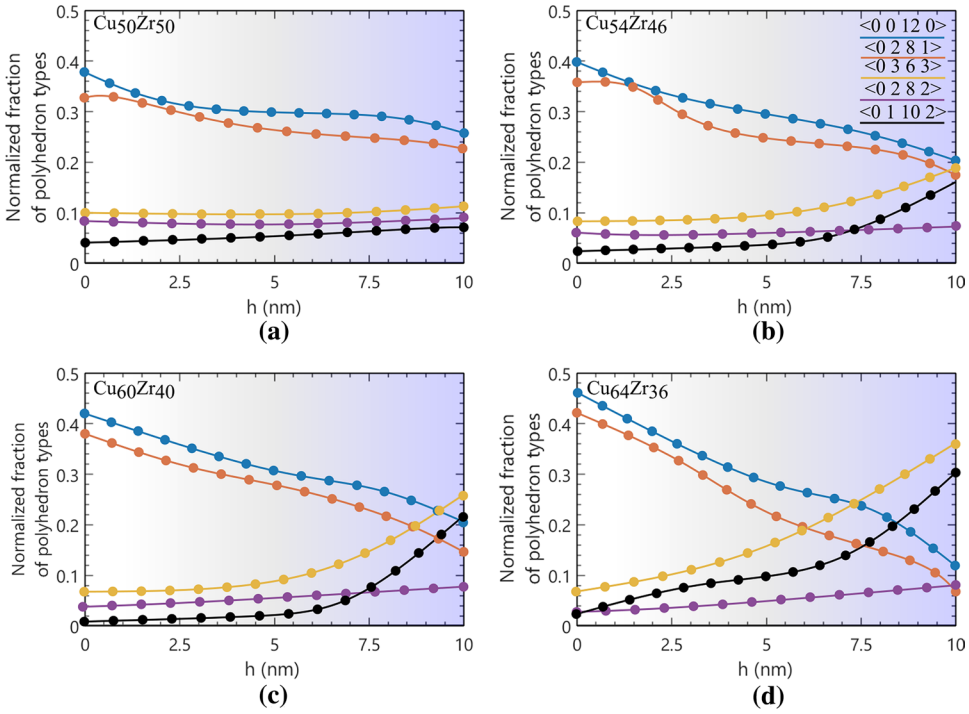

Fig. 8 The variations of polyhedron types during the indenting process for **a** $Cu_{50}Zr_{50}$, **b** $Cu_{54}Zr_{46}$, **c** $Cu_{60}Zr_{40}$ and **d** $Cu_{64}Zr_{36}$

This result indicated that the brittle localized deformation in the Cu-rich MGs are associated with the sharp annihilation of ⟨0, 0, 12, 0⟩ polyhedron and the intensified creation of ⟨0 1 10 2⟩ and ⟨0, 2, 8, 2⟩ clusters. While, the decrease of Cu content is accompanied with the moderate increment/decrement of polyhedrons in the system (see Fig. 8). In summary, it is concluded that the evolution of deformation under the indenting process strongly relies on the chemical composition of MGs, so that a slight change in the elements leads to a significant impact on the mechanical response of material to the applied loads.

4 Conclusions

In this work, the nanomechanical properties of CuZr MGs was evaluated by the MD simulation. The results indicated that the rise of Cu content in the alloying composition led to the increment of yielding force in the MGs. On the other side, an optimized composition, i.e. $Cu_{60}Zr_{40}$, was identified for the maximum hardening effect in the glassy structure. Moreover, with the increase of Zr content, i.e. $Cu_{50}Zr_{50}$, the shear bands accumulatively propagated into the depth of glassy structure without any significant extension at the surface of sample. Whereas, the Cu-rich MGs included the pile-up shear events around the indenting site and the subsequent dominant shear bands propagated into the sample. Furthermore, the Voronoi analysis demonstrated that the indenting process was accompanied with the decrease of ⟨0 0 12 0⟩ polyhedron along with the decrease of ⟨0 2 8 2⟩ and ⟨0 1 10 2⟩ polyhedrons in all the samples; however, the rate of decreasing/increasing trends strongly depended on the chemical composition.

References

1. J.W. Lv, F.L. Wang, D.W. Yin, S. Zhang, Z.Q. Cai, Z.L. Shi, M.Z. Ma, X.Y. Zhang, J. Alloy. Compd. **887**, 161386 (2021)
2. M. Sadeghilaridjani, A. Ayyagari, S. Muskeri, V. Hasannaeimi, J. Jiang, S. Mukherjee, JOM. **72**, 123 (2020)
3. M. Samavatian, R. Gholamipour, A.A. Amadeh, S. Mirdamadi, Metall. Mater. Trans. A **50**, 4743 (2019)
4. S. Di, Q. Wang, J. Zhou, Y. Shen, J. Li, M. Zhu, K. Yin, Q. Zeng, L. Sun, B. Shen, Scripta Mater. **187**, 13 (2020)
5. M. Samavatian, R. Gholamipour, A.A. Amadeh, S. Mirdamadi, Mater. Sci. Eng. A **753**, 218 (2019)
6. X. Mu, M.R. Chellali, E. Boltynjuk, D. Gunderov, R.Z. Valiev, H. Hahn, C. Kübel, Y. Ivanisenko, L. Velasco, Adv. Mater. **33**, 2007267 (2021)
7. D. Sorensen, E. Hintsala, J. Stevick, J. Pischlar, B. Li, D. Kiener, J.C. Myers, H. Jin, J. Liu, D. Stauffer, A.J. Ramirez, R.O. Ritchie, Acta Mater. **183**, 242 (2020)
8. J. Pan, Y.P. Ivanov, W.H. Zhou, Y. Li, A.L. Greer, Nature **578**, 559 (2020)
9. Q. Zhu, M. Zhang, X. Jin, H. Yang, L. Jia, J. Qiao, J. Mater. Res. **36**, 2047 (2021)
10. S.Y. Chau, S. To, Z. Sun, H. Wu, Int. J. Adv. Manuf. Technol. **107**, 4437 (2020)
11. S.S. Jiang, K.F. Gan, Y.J. Huang, P. Xue, Z.L. Ning, J.F. Sun, A.H.W. Ngan, Int. J. Plasticity **125**, 52 (2020)
12. T.-X. Bui, T.-H. Fang, C.-I. Lee, Physica B **583**, 412021 (2020)
13. J. Ge, H. He, J. Zhou, C. Lu, W. Dong, S. Liu, S. Lan, Z. Wu, A. Wang, L. Wang, C. Yu, B. Shen, X.-l. Wang, J. Alloy. Compd. **787**, 831 (2019)

14. C. Liu, V. Roddatis, P. Kenesei, R. Maaß, Acta Mater. **140**, 206 (2017)
15. K. Tao, J.C. Qiao, Q.F. He, K.K. Song, Y. Yang, Int. J. Mech. Sci. **201**, 106469 (2021)
16. K.P. Marimuthu, K. Lee, J. Han, F. Rickhey, H. Lee, J. Mater. Res. Technol. **9**, 104 (2020)
17. Z.Y. Ding, Y.X. Song, Y. Ma, X.W. Huang, T.H. Zhang, Metals **9**, 613 (2019)
18. Y. Wang, J. Zhang, K. Wu, G. Liu, D. Kiener, J. Sun, Mater. Res. Lett. **6**, 22 (2018)
19. H. Huang, J. Yan, Mater. Sci. Eng. A **704**, 375 (2017)
20. H. Huang, M. Jiang, J. Yan, J. Alloy. Compd. **857**, 157587 (2021)
21. F. Dong, M. He, Y. Zhang, L. Luo, Y. Su, B. Wang, H. Huang, Q. Xiang, X. Yuan, X. Zuo, B. Han, Y. Xu, Int. J. Hydrogen Energ. **42**, 25436 (2017)
22. Y. Du, Q. Zhou, Y. Ren, W. Kuang, W. Han, S. Zhang, H. Zhai, H. Wang, J. Alloy. Compd. **762**, 422 (2018)
23. M. Liu, D. Hou, C. Gao, J. Non. Cryst. Solids **561**, 120750 (2021)
24. M. Gao, J.H. Perepezko, Mater. Sci. Eng. A **801**, 140402 (2021)
25. W.-P. Wu, D. Şopu, X. Yuan, J. Eckert, J. Appl. Phys. **128**, 084303 (2020)
26. C. Qiu, P. Zhu, F. Fang, D. Yuan, X. Shen, Appl. Surf. Sci. **305**, 101 (2014)
27. D. Zhao, B. Zhu, S. Wang, Y. Niu, L. Xu, H. Zhao, Comput. Mater. Sci. **186**, 110073 (2021)
28. M.I. Mendelev, D.J. Sordelet, M.J. Kramer, J. Appl. Phys. **102**, 043501 (2007)
29. A.H. Neelav, S. Pal, C. Deng, J. Appl. Phys. **126**, 125101 (2019)
30. L. Si, D. Guo, J. Luo, G. Xie, Appl. Phys. A **109**, 119 (2012)
31. Y. Tian, Q. Fang, J. Li, Nanotechnology **31**, 465701 (2020)
32. J. Li, B. Lu, Y. Zhang, H. Zhou, G. Hu, R. Xia, Mater. Chem. Phys. **241**, 122391 (2020)
33. H.-T. Luu, S.-L. Dang, T.-V. Hoang, N. Gunkelmann, Appl. Surf. Sci. **551**, 149221 (2021)
34. C.L. Kelchner, S.J. Plimpton, J.C. Hamilton, Phys. Rev. B **58**, 11085 (1998)
35. K. Kremer, G.S. Grest, J. Chem. Phys. **92**, 5057 (1990)
36. S. Cheng, E. Phillips, L. Parks, Radiat. Phys. Chem. **79**, 329 (2010)
37. J.H. Kim, Y.H. Kim, Comput. Mech. **29**, 441 (2002)
38. Z.T. Wang, J. Pan, Y. Li, C.A. Schuh, Phys. Rev. Lett. **111**, 135504 (2013)
39. C. Liu, A. Das, W. Wang, S. Küchemann, P. Kenesei, R. Maaß, Scripta Mater. **170**, 29 (2019)
40. M. Huráková, K. Csach, A. Juríková, J. Miškuf, Š Demčák, V. Ocelík, J.T.M. De Hosson, J. Non Cryst. Solids **470**, 160 (2017)
41. D. Zhao, H. Zhao, B. Zhu, S. Wang, Appl. Surf. Sci. **416**, 14 (2017)
42. F. Dong, M. He, Y. Zhang, B. Wang, L. Luo, Y. Su, H. Yang, X. Yuan, Mater. Sci. Eng. A **759**, 105 (2019)
43. C. Ma, S. Li, P. Huang, F. Wang, J. Non Cryst. Solids **534**, 119953 (2020)
44. H. Huang, J. Yan, Appl. Surf. Sci. **462**, 565 (2018)
45. S.X. Song, X.-L. Wang, T.G. Nieh, Scripta Mater. **62**, 847 (2010)
46. R.T. Qu, S.G. Wang, G.J. Li, R.F. Wang, X.D. Wang, S.J. Wu, Z.F. Zhang, Scripta Mater. **162**, 136 (2019)
47. R. Maaß, J.F. Löffler, Adv. Funct. Mater. **25**, 2353 (2015)
48. S.D. Mesarovic, N.A. Fleck, Proc. R. Soc. Lond. A Math. Phys. **455**, 2707 (1999)
49. A. Lee, K. Komvopoulos, Int. J. Solids Struct. **146**, 180 (2018)
50. T. Zhang, W. Cheng, G. Peng, Y. Ma, W. Jiang, J. Hu, H. Chen, MRS Commun. **9**, 360 (2019)
51. P. Thurnheer, F. Haag, J.F. Löffler, Acta Mater. **115**, 468 (2016)
52. A. Das, P. Kagebein, S. Küchemann, R. Maaß, Appl. Phys. Lett. **112**, 261905 (2018)
53. I. Binkowski, G.P. Shrivastav, J. Horbach, S.V. Divinski, G. Wilde, Acta Mater. **109**, 330 (2016)
54. S. Feng, L. Li, K.C. Chan, L. Zhao, L. Wang, R. Liu, J. Mater. Sci. Technol. **43**, 119 (2020)